Gravity Currents Propagating on Sloping Boundaries

Albert Dai[1]

Abstract: Three-dimensional direct numerical simulations of gravity currents on different bottom slopes are presented in this paper. After the buoyancy closed in a lock is instantaneously released, the produced gravity currents go through an acceleration phase followed by a deceleration phase. In the acceleration phase, the tail current connects to and feeds buoyancy into the head for all cases considered here. The maximum buoyancy contained in the head, reached at the end of the acceleration phase, increases as the bottom slope increases. The maximum buoyancy in the head never reaches the total released buoyancy, and a significant portion of released heavy fluid is left in the tail current. In the deceleration phase, the tail current continues to join the head as the gravity currents propagate for lower slope angles ($\theta = 0.2$, and 4°), but the head disconnects the joining tail current for higher slope angles ($\theta = 6$, 8, and 10°). The gravity current head loses contained buoyancy less rapidly in the deceleration phase as the bottom slope increases. Structures of the gravity current indicate that the relative length of the head diminishes as the gravity currents propagate downslope for lower slope angles and remains approximately constant for higher slope angles. The maximum front velocity increases as the bottom slope increases. In the deceleration phase, the front location–time relationship follows the thermal theory power law for higher slope angles and for lower slope angles, and the inertial phase power-law asymptote is observed. **DOI: 10.1061/(ASCE)HY.1943-7900.0000716.**

CE Database subject headings: Currents; Thermal factors; Slopes; Simulation; Three-dimensional models.

Author keywords: Gravity currents; Buoyancy-driven flows; Thermal theory.

Introduction

Gravity currents, otherwise known as buoyancy or density currents, are flows driven by a density difference. The density difference may be due to temperature differentials or dissolved and suspended materials, e.g., salt and sediments. The majority of works on gravity currents have focused on a finite buoyancy instantaneously released on a horizontal boundary, i.e., lock-exchange flows (Simpson 1997; Shin et al. 2004; La Rocca et al. 2008). Gravity currents down a slope are less considered in the literature but are also commonly encountered in geophysical environments and engineering applications. Readers are referred to Allen (1985), Fannelop (1994), and Simpson (1997) for more details about gravity currents and a review of the great diversity of possible cases.

Related to the present study, Britter and Linden (1980) considered continuously maintained density flow down slopes at angles varying from 5 to 90° and reported a steady front velocity for gravity currents produced from a continuous buoyancy source when the slope is greater than 0.5°. For gravity currents produced from a finite, instantaneous buoyancy source, the Laboratory of Geophysical and Industrial Flows (LEGI) group at the University of Grenoble in Grenoble, France, and collaborators have performed a series of experiments aimed at modeling powder-snow avalanches and turbidity currents down the continental slope to the deep ocean, and in these examples the flow domain is essentially infinite with a free surface (Hopfinger and Tochon-Danguy 1977; Beghin et al. 1981; Rastello and Hopfinger 2004). In summary, their experiments showed that, after released on a slope, gravity currents first go through an acceleration phase followed by a deceleration phase. These works differ from full-depth, lock-exchange experiments in that the initial buoyancy and subsequent flows occupy a sufficiently small fraction of the flow domain and the influence of the top boundary is considered negligible. Therefore, the top boundary was set parallel to the bottom boundary in previous work. For example, the initial height of the heavy fluid in Beghin et al. (1981) was 16% of the total domain height, and the height of the produced gravity current head on a 5° slope therein remained less than 20% of the domain height. In addition, the thermal theory was developed in that work by Beghin et al. (1981) following the noted Morton et al. (1956) to describe the front velocity history and has formed the basis for many subsequent studies (see, for example, the references in Dai 2010). Recently, Maxworthy and Nokes (2007) reported that for gravity currents produced from a slender body of initial heavy fluid, with the long side lying on the slope, the acceleration phase is extended like a continuous line plume, and they modified the thermal theory to account for the influence of buoyancy increase on the gravity current propagation. In our case, the initial heavy fluid that is set following Beghin et al. (1981) is more compact. As discussed and estimated in Maxworthy and Nokes (2007), approximately 30% of the initial heavy fluid in a lock would be available to feed the gravity current head on a 10° slope, and as such the acceleration phase would be significantly shortened. In the deceleration phase, Maxworthy (2010) reported that the head began to lose buoyancy-containing fluid from its rear by detrainment.

The configuration of the problem is sketched in Fig. 1. Here the density of ambient fluid is taken as $\tilde{\rho}_0$ and the density of initial heavy fluid is $\tilde{\rho}_1$, where $(\tilde{\rho}_1 - \tilde{\rho}_0)/\tilde{\rho}_0 \ll 1$. After an instantaneous release of heavy fluid from a lock, the head of the gravity current forms a self-similar semielliptical shape with a constant height-to-length aspect ratio $\kappa = \tilde{H}/\tilde{L}$. Based on the thermal theory, the height and length of the gravity current head are

[1]Dept. of Water Resources and Environmental Engineering, Tamkang Univ., New Taipei City 25137, Taiwan. E-mail: hdai@mail.tku.edu.tw

Note. This manuscript was submitted on April 8, 2012; approved on December 5, 2012; published online on December 7, 2012. Discussion period open until November 1, 2013; separate discussions must be submitted for individual papers. This paper is part of the ***Journal of Hydraulic Engineering***, Vol. 139, No. 6, June 1, 2013. © ASCE, ISSN 0733-9429/2013/6-593-601/$25.00.

$$\tilde{H} = \frac{1}{2}\frac{S_2}{S_1}\kappa^{1/2}\alpha(\tilde{x}+\tilde{x}_0), \qquad \tilde{L} = \frac{1}{2}\frac{S_2}{S_1}\kappa^{-1/2}\alpha(\tilde{x}+\tilde{x}_0) \tag{1}$$

where $S_1 = \pi/4$ and $S_2 = (\pi/2^{3/2})(4\kappa^2+1)^{1/2}/\kappa^{1/2}$ are the shape factors, α is the entrainment coefficient (Ellison and Turner 1959), $\tilde{x}$ is the distance from the left wall ($x_1 = 0$) to the mass center of the head, and $\tilde{x}_0$ is the distance measured from the fictitious virtual origin to the left wall. With Boussinesq approximations, the mass-center velocity of the gravity current head is derived from the momentum equation as

$$\tilde{U} = \left[\frac{2}{3}C\frac{1}{\tilde{x}+\tilde{x}_0}\left(1-\left(\frac{\tilde{x}_0}{\tilde{x}+\tilde{x}_0}\right)^3\right)\right]^{1/2} \tag{2}$$

when the heavy fluid is released from the quiescent initial state. Here $C = (4S_1\tilde{B}\sin\theta)/[(1+k_v)\alpha^2 S_2^2]$, $\tilde{B} = \tilde{g}(\tilde{\rho}-\tilde{\rho}_0)S_1\tilde{H}\tilde{L}/\tilde{\rho}_0$ is the total buoyancy, and $k_v = 2k$ is the added mass coefficient (Batchelor 1967). With the geometric relation for the gravity current head, $\tilde{x}_f = \tilde{x}+\tilde{L}/2$, the front velocity is related to the mass-center velocity by $\tilde{U}_f = [1+\alpha S_2/(4S_1\kappa^{1/2})]\tilde{U}$. Although analytically simple, Eq. (2) outlines the behavior of a gravity current down a slope and predicts that the front velocity will increase as the buoyancy contained in the head and the bottom slope increase since both factors lead to increasing values of C. Following Beghin et al. (1981), for large values of $\tilde{x}$, i.e., $(\tilde{x}/\tilde{x}_0) \gg 1$,

$$\tilde{H} \sim \tilde{x}_f, \qquad \tilde{L} \sim \tilde{x}_f, \qquad \tilde{U}_f \sim \tilde{x}_f^{-1/2} \tag{3}$$

Alternatively, Maxworthy (2010) recast the relation between front location and time in the following form:

$$(\tilde{x}_f+\tilde{x}_0) = K_M\tilde{B}_0^{1/3}(\tilde{t}+\tilde{t}_0)^{2/3} \tag{4}$$

where K_M = a constant yet to be determined and $\tilde{B}_0$ = an experimental setup constant. When $\tilde{x}_f \gg \tilde{x}_0$ and $\tilde{t} \gg \tilde{t}_0$, i.e., when the gravity current is sufficiently far into the deceleration phase, the asymptotic velocity-distance relation in Eq. (3) is recovered. It was also reported in Maxworthy (2010) that the power-law Eq. (4) is robust even when the conditions $\tilde{x}_f \gg \tilde{x}_0$ and $\tilde{t} \gg \tilde{t}_0$ are not satisfied.

Coincidentally, for planar gravity currents produced from a lock exchange on a horizontal boundary, Huppert and Simpson (1980) showed that after the constant-velocity slumping phase, the front velocity satisfies the relationships

$$\tilde{U}_f \sim \tilde{t}^{-1/3} \quad \text{and} \quad \tilde{x}_f \sim \tilde{t}^{2/3} \tag{5}$$

during the inertial phase for full-depth releases; similar results were also obtained for partial-depth releases (Marino et al. 2005). Note that the power-law asymptote for the inertial phase is equivalent to the thermal theory prediction provided the gravity current is sufficiently far from the virtual origin. After the inertial phase there exists a viscous phase in which the following front velocity asymptotics were obtained:

$$\tilde{U}_f \sim \tilde{t}^{-5/8} \quad \text{and} \quad \tilde{x}_f \sim \tilde{t}^{3/8} \tag{6}$$

A previous numerical study of gravity currents on a 10° slope was carried out by Dai et al. (2012), and it was shown that the buoyancy contained in the head was at most approximately 58% of the total released buoyancy, and an upslope propagating tail current was observed. However, the heavy fluid was set in motion by instantaneously removing all the enclosing walls in Dai et al. (2012), and as such an upslope propagating current was generated, whereas in reported experiments, only the front gate was removed and the released heavy fluid propagated unidirectionally downslope. To account for the initiation mechanism of gravity currents in experiments and to study how the characteristics of gravity currents change as the bottom slope increases from 0 to 10°, the problem of Beghin et al. (1981) was reinvestigated using direct numerical simulations (DNS), in which all scales of motion were fully resolved in space and time. While four Reynolds numbers were reported in Dai et al. (2012), only $\mathrm{R} = 10^4$ is chosen here because this is sufficiently large for gravity currents in the turbulent flow regimes and the provided numerical resolution is consistent with the present authors' computational resources.

Numerical Formulation

Fig. 1 shows half of the configuration of gravity current simulations. To ensure a reflection condition at the midplane ($x_1 = 0$) as in experiments and to prevent any upslope propagating currents, the other half is a symmetric image placed to the left of the configuration shown in Fig. 1. In the figure, the computational domain of interest is chosen as $L_{x_1} \times L_{x_2} \times L_{x_3} = 12 \times 3 \times 2$ and the buoyancy initially occupies the shaded region of $l_0 \times h_0 = 0.4 \times 0.32$ without momentum. At $t = 0$, the buoyancy is instantaneously released and allowed to propagate downstream. Streamwise, spanwise, and wall-normal directions follow the right-hand rule and are denoted by x_1, x_2, and x_3, respectively. The channel is tilted so the gravity vector $\tilde{e}_i^g$ makes an angle θ with the wall-normal direction, x_3. Simulations of gravity currents on bed slopes, $\theta = 0$, 2, 4, 6, 8, 10°, are performed in the study. H and L are the height and length of the gravity current head, and the front location is denoted by x_f measured from the left wall in the figure (x_1). The virtual origin, which is identified through extrapolation to $H = 0$, is located x_0 beyond the wall. The heavy fluid of density $\tilde{\rho}_1$ is confined in the locked region and separated from the light fluid of density $\tilde{\rho}_0$. Here we assume that the density difference is small enough so that Boussinesq approximations can be adopted. The governing equations, i.e., conservation of mass, momentum, and buoyancy,

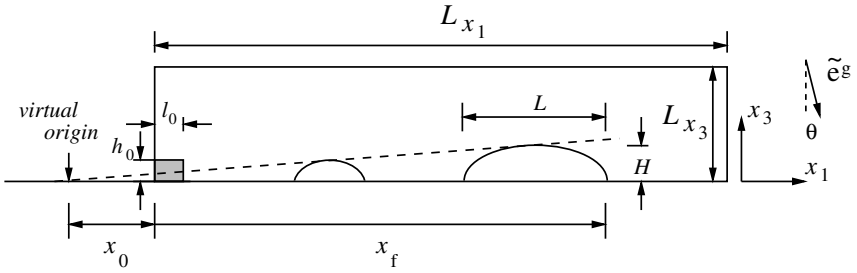

Fig. 1. Sketch of gravity current propagating on a sloping boundary

J. Hydraul. Eng., 2013, 139(6): 593-601

where the influence of density variations is neglected in the inertia term but retained only in the buoyancy term, take the dimensionless form

$$\frac{\partial u_k}{\partial x_k} = 0 \tag{7}$$

$$\frac{\partial u_i}{\partial t} + \frac{\partial (u_i u_k)}{\partial x_k} = \rho e_i^g - \frac{\partial p}{\partial x_i} + \frac{1}{Re}\frac{\partial^2 u_i}{\partial x_k \partial x_k} \tag{8}$$

$$\frac{\partial \rho}{\partial t} + \frac{\partial (\rho u_k)}{\partial x_k} = \frac{1}{ReSc}\frac{\partial^2 \rho}{\partial x_k \partial x_k} \tag{9}$$

Here u_i = velocity vector; ρ = density; e_i^g = unit vector pointing in gravity direction; and p = pressure. In the present study the channel is inclined at an angle θ; therefore, $e_i^g = (\sin\theta, 0, -\cos\theta)^T$. The variables in Eqs. (7)–(9) are made dimensionless by the channel half-height, $\tilde{h}$, as the length scale and the buoyancy velocity, $\tilde{u}_b = \sqrt{\tilde{g}'\tilde{h}}$, as the velocity scale, where the reduced gravity $\tilde{g}'$ is

$$\tilde{g}' = \tilde{g}\frac{\tilde{\rho}_1 - \tilde{\rho}_0}{\tilde{\rho}_0} \tag{10}$$

The choice of channel half-height as the length scale here is for computational purposes (Canuto et al. 1988; Hartel et al. 2000; Cantero et al. 2007; Dai et al. 2012). As will be explained subsequently, in the wall-normal direction we employ the Chebyshev expansion, which requires that the computational domain in the wall-normal direction be between −1 and 1. However, it should be remarked that $(\tilde{h}_0\tilde{l}_0)^{1/2}$ is a relevant and commonly used physical length scale in the problem. The dimensionless pressure and density are given by

$$p = \frac{\tilde{p}}{\tilde{\rho}_0 \tilde{u}_b^2}, \qquad \rho = \frac{\tilde{\rho} - \tilde{\rho}_0}{\tilde{\rho}_1 - \tilde{\rho}_0} \tag{11}$$

According to our nondimensionalization scheme, the dimensionless density is in the range $0 \le \rho \le 1$. At $t = 0$, the heavy fluid occupies the region of $\rho = 1$ and the ambient fluid region is represented by that of $\rho = 0$. The initial density contrast, $\tilde{\rho}_1 - \tilde{\rho}_0$, only comes into play via the reduced gravity $\tilde{g}'$ and is specified implicitly via the Reynolds number. The Reynolds number and the Schmidt number arising from the nondimensionalization of the equations are defined by

$$\mathrm{R} = \frac{\tilde{u}_b \tilde{h}}{\tilde{\nu}}, \qquad \mathrm{Sc} = \frac{\tilde{\nu}}{\tilde{\kappa}} \tag{12}$$

respectively, where $\tilde{\nu}$ represents the kinematic viscosity and $\tilde{\kappa}$ the diffusivity of the density field. Based on the observation that the influence of Schmidt number on the flow is weak, we employed $\mathrm{Sc} = 1$ in all simulations (Hartel et al. 2000; Bonometti and Balachandar 2008).

In the present investigation the code described in Cortese and Balachandar (1995) based on the dealiased pseudospectral method (Canuto et al. 1988) is employed and a detailed validation of the code for lock-exchange flows is given in Cantero et al. (2006, 2007). As introduced earlier, the code was modified in Dai et al. (2012) for gravity currents on a slope, but an upslope propagating tail current was generated due to the imperfect initiation mechanism. To more accurately model the lock configuration in experiments, where only one end facing the downstream direction is instantly open, here we impose a reflection condition at the streamwise midplane ($x_1 = 0$) such that the heavy fluid in the lock fully spreads into the channel of length L_{x_1}. The governing equations are solved in a rectangular domain $2L_{x_1} \times L_{x_2} \times L_{x_3}$ with resolution $N_{x_1} \times N_{x_2} \times N_{x_3}$. The width of the channel was chosen to be $L_{x_2} = 3$, which is sufficient for spanwise variation, including several lobe and cleft structures (Hartel et al. 2000). The channel length in the streamwise direction was chosen to be $L_{x_1} = 12$ to allow for the full development of acceleration and deceleration phases and comparison with Beghin et al. (1981). To achieve spectral accuracy, periodic boundary conditions are employed in the streamwise and spanwise directions,

$$f(x_1, x_2, x_3, t) = \sum_{k_1, k_2} \hat{f}_{k_1,k_2}(x_3, t) e^{i\pi k_1 x_1 / L_{x_1}} e^{i2\pi k_2 x_2 / L_{x_2}} \tag{13}$$

where f = discretized variables, namely, the velocity components, pressure, and density, and $\hat{f}$ = coefficients of Fourier transforms. Streamwise periodicity implies that an array of planar gravity currents, each separated by $2L_{x1}$ initially, is being simulated. The wavenumbers in the x_1- and x_2-directions are k_1 and k_2, respectively, which satisfy

$$|k_1| \le \frac{N_{x_1}}{2}, \qquad |k_2| \le \frac{N_{x_2}}{2} \tag{14}$$

In the wall-normal direction, we employ the Chebyshev expansion for $\hat{f}$ with Gauss-Lobatto quadrature points, which provide higher resolution near the walls and allow for straightforward treatment of boundary conditions. Using Gauss-Lobatto quadrature points also implies that the top boundary is parallel to the bottom boundary, rather than simply horizontal as a free surface. However, because the initial heavy fluid is enclosed in a small region, consistent with previous work, the influence of the top boundary on the gravity currents is assumed to be negligible, as confirmed by the investigation of Beghin et al. (1981). At the top and bottom boundaries, $x_3 = \pm 1$, the no-slip and no-flux conditions are employed for the velocity and density fields, i.e.,

$$u_i = 0, \qquad \frac{\partial \rho}{\partial x_3} = 0 \quad \text{at } x_3 = \pm 1 \tag{15}$$

To solve the equations in the velocity-pressure formulation, the diffusion terms are treated implicitly using the Crank-Nicolson scheme. The convection and buoyancy-forcing terms are treated explicitly using the low-storage third-order Runge-Kutta scheme (Williamson 1980). The Arakawa method (Durran 1999), in which the convective and divergence forms of the nonlinear term are alternately used, is also employed for the convection term to reduce the aliasing error. In all simulations, the velocity field was initialized with fluid at rest, i.e., $u_i = 0$ everywhere. The initial density field is prescribed to be unity in the heavy fluid region and zero in the light fluid region, with a steep error-function-type transition between the two values. The initial density field is also seeded with a minute random disturbance to ensure transition to turbulence (Cantero et al. 2006). In this paper, we present three-dimensional DNS at $\mathrm{R} = 10^4$ and observe the influence of the bottom slope by choosing $\theta = 0$, 2, 4, 6, 8, and 10°. The Reynolds number ($\mathrm{R} = 10^4$) is chosen such that the gravity currents are in the turbulent flow regimes while the provided numerical resolution is consistent with our computational resources. To fully resolve the largest and smallest scales of the gravity current motion in the computational domain ($2L_{x_1} \times L_{x_2} \times L_{x_3} = 24 \times 3 \times 2$), the numerical mesh $N_{x_1} \times N_{x_2} \times N_{x_3} = 840 \times 128 \times 220$ was selected for all simulations. The chosen spatial resolution is consistent with the requirement that the grid size be of the order of $O(1/\sqrt{\mathrm{RSc}})$

(Birman et al. 2005, 2007) and follows Dai et al. (2012). The time step was chosen to produce a Courant number less than 0.5.

Results

Flow Characteristics

When the gravity currents produced from an instantaneous buoyancy source propagate on inclined boundaries, they exhibit a structure with a distinct head and a following tail current. For easy visualization of the gravity current and for an unambiguous measure of buoyancy, the width-averged density, $\bar{\rho}$, and the equivalent height, $\bar{h}$, are defined as

$$\bar{\rho}(x_1, x_3, t) = \frac{1}{L_{x_2}} \int_0^{L_{x_2}} \rho(x_1, x_2, x_3, t) dx_2,$$
$$\bar{h}(x_1, t) = \int_{-1}^{1} \bar{\rho}(x_1, x_3, t) dx_3 \tag{16}$$

respectively (Shin et al. 2004; Marino et al. 2005; Cantero et al. 2007). To illustrate the concept of equivalent height, in fluid columns filled entirely by the light ambient fluid, the equivalent height is zero; in fluid columns filled entirely by the released heavy fluid, the equivalent height is L_{x_3}. The equivalent height provides a clear measure of the distribution of heavy fluid in the streamwise direction; however, the equivalent height is distinct from the height of the gravity current head, H, which is defined using the width-averaged density $\bar{\rho}$ (Dai et al. 2012). According to the configuration shown in Fig. 1, the total released buoyancy in the channel is given by

$$\int_0^{L_{x_1}} \bar{h}(x_1, t) dx_1 = h_0 l_0 \quad \forall\ t \tag{17}$$

As an example, the flow field is visualized in Fig. 2 by the width-averaged density, $\bar{\rho}$, for the gravity current propagating on a 10° slope at $\mathsf{R} = 10^4$. The startup roller forming as the heavy fluid slumps at the initial stage of gravity current propagation is observed in Fig. 2(a). Fig. 3 shows the evolutions of the equivalent height for gravity currents on different slopes. Moreover, the gravity current head not only moves downslope but also spreads simultaneously, as indicated by the decreasing equivalent height. Using the results in Fig. 3, the front location, x_f, can be identified without ambiguity. Here the front of the current is taken to be at the location given by $\bar{h} = 0.001$, and due to the sharpness of the density gradient, the location of the front is insensitive to the actual value of $\bar{h}$ chosen to identify it.

Of particular interest here is the growth of the height and length of the gravity current head. To define the length and height of the head, we take advantage of the width-averaged density, illustrated in Fig. 2(f), in that the semielliptical head is marked by a height, H, and length, L, and is separated from the tail current by a local indentation. As shown in Fig. 4, during the initial developing stage of gravity current motion, the height and length of the gravity current head both increase linearly with downslope distance. Note that the rate of size increase depends on the slope angle, where the increase rate in the height is more sensitive than the length. At $\theta = 10°$, the approximate relationships H:0.07x_f and L:0.32x_f are in agreement with reported experimental observations (Beghin et al. 1981). However, the height of the head ceases to increase linearly as in the initial stage at x_f:2.5 and grows less rapidly with distinct mild undulation. By extrapolating the gravity current height and distance relationship in Fig. 4(a), the virtual origin can be identified for the deceleration phase at higher slope angles ($\theta = 6$, 8, and 10°), but

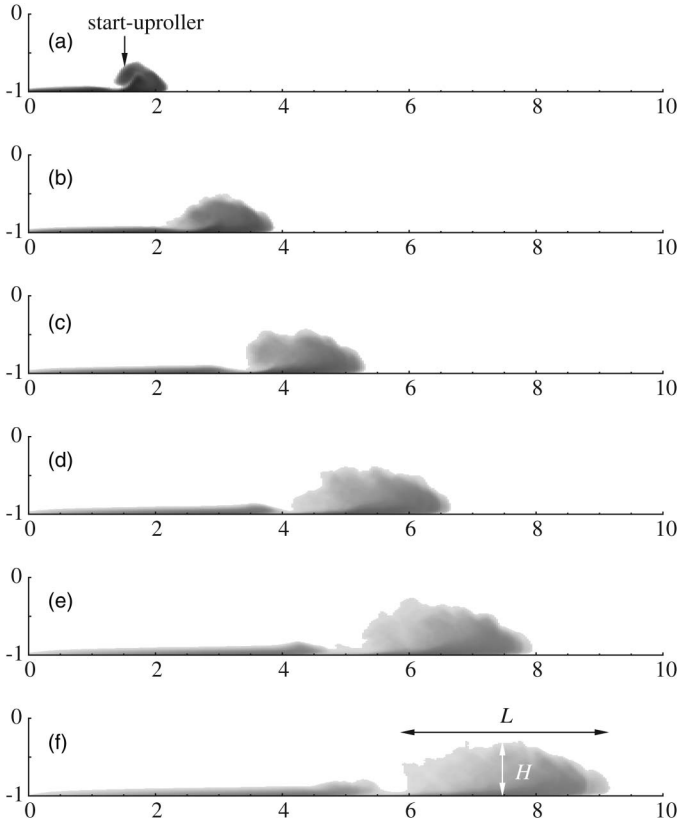

Fig. 2. Flow evolutions visualized by width-averaged density, $\bar{\rho}$, for gravity current propagating on a 10° slope at $\mathsf{R} = 10^4$; (a)–(f) are chosen at $t = 5$, 10, 15, 20, 25, 30 dimensionless time units

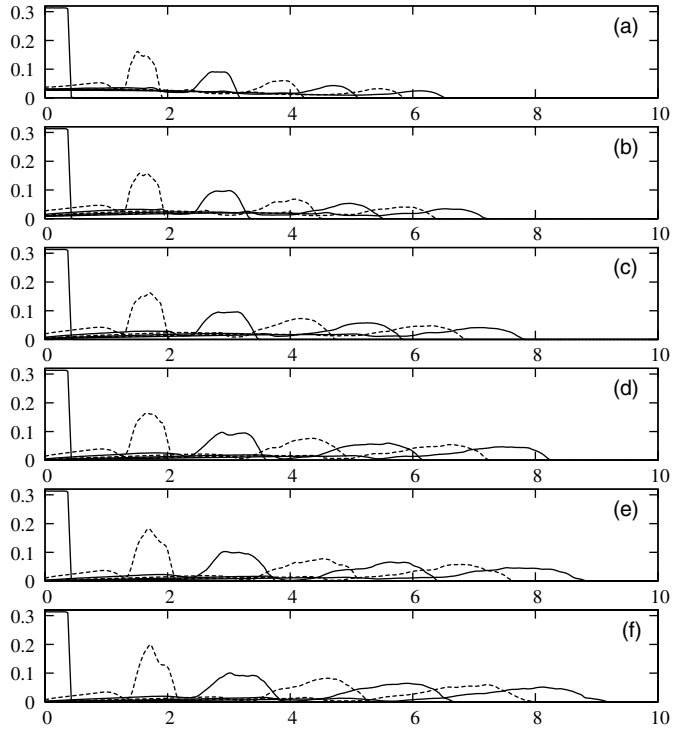

Fig. 3. Equivalent heights of gravity currents at $\mathsf{R} = 10^4$ produced from a finite buoyancy source on different slope angles: (a) $\theta = 0°$; (b) $\theta = 2°$; (c) $\theta = 4°$; (d) $\theta = 6°$; (e) $\theta = 8°$; (f) $\theta = 10°$; time interval between consecutive instances in each frame is five dimensionless time units

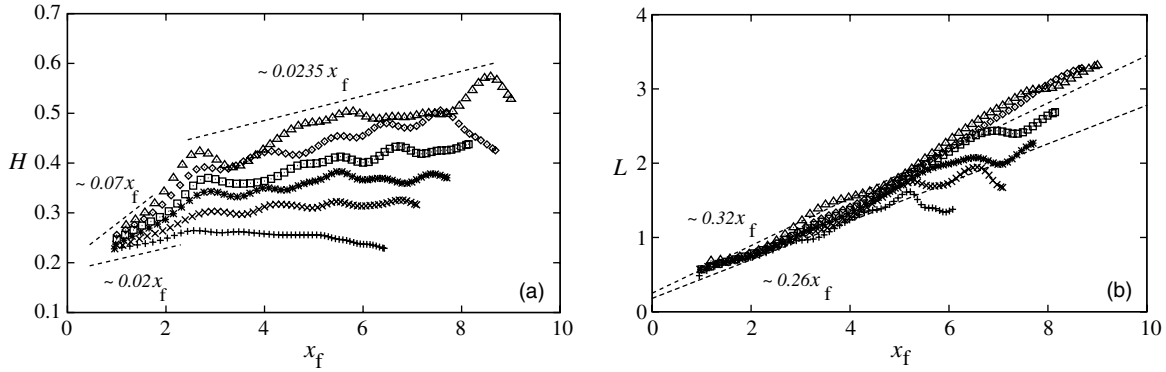

Fig. 4. (a) Height and (b) length of gravity current head versus downslope distance, x_f; symbols: plus symbol, $\theta = 0°$; x-shaped symbol, $\theta = 2°$; asterisk, $\theta = 4°$; square, $\theta = 6°$; diamond, $\theta = 8°$; triangle, $\theta = 10°$; relationships between the size and distance, H:$0.07x_f$ and L:$0.32x_f$, are consistent with reported experimental observations for $\theta = 10°$ in Beghin et al. (1981)

for lower slope angles ($\theta = 0$, 2, and 4°) finding the virtual origin becomes infeasible because the current height is essentailly constant or decreasing in the deceleration phase.

Fig. 5 shows the gravity current structures on a stretched coordinate normalized by x_f. Note that for lower slope angles ($\theta = 0$, 2, and 4°), the head is constantly connected with the tail current and the relative length of the head, L/x_f, diminishes as the gravity current propagates downslope; for higher slope angles ($\theta = 6$, 8, and 10°), the head is distinct from the tail, and after the head is clearly formed (at t:5), the relative length of the head remains approximately constant ($L/x_f \approx 0.35$). Fig. 5 also shows that the distribution of heavy fluid contained within the head moves toward the downslope side as the gravity current propagates.

Fig. 6 shows the aspect ratio, k, versus the downslope distance. Following Morton et al. (1956), the self-similarity assumption for the semielliptical front in thermal theory requires the aspect ratio to be a constant. However, detailed inspection shows that the aspect ratio steadily decreases as the gravity current propagates downslope, e.g., from approximately 0.4 when the semielliptical front develops to less than 0.2 after $x_f = 6$ for $\theta = 10°$, for all the bottom slopes considered in the study.

Front Velocity

The front velocity, u_f, can be obtained from the time dependence of the front location x_f as

$$u_f = \frac{dx_f}{dt} \tag{18}$$

Fig. 7(a) first shows the front location versus time for all the cases considered here. Detailed relationships for the initial acceleration and deceleration phases are shown in Figs. 7(b and c), respectively. It is obvious from Figs. 7(a and b) that the gravity currents propagate at a speed that increases with the bottom slope. To clarify the influence of no-slip conditions at the top boundary, a simulation with a free-slip top for $\theta = 10°$ was run and included in Fig. 7. It is observed that except for the later stage in the deceleration phase ($t > 15$), the propagation of gravity currents with a free-slip top is consistent with that with a no-slip top boundary in the acceleration phase and early deceleration phase. Note that in Britter and Linden (1980), the front velocity is found to be a constant proportional to the cube root of the buoyancy flux and almost independent of the slope provided the slope angle is greater than 0.5°. The is because a balance between the continuously supplied buoyancy flux and entrainment of ambient fluid is struck in Britter and Linden (1980), while in the present study, the gravity currents evolve into the deceleration phase due to the finite volume of released buoyancy. Fig. 7(c), plotted on a log-log scale, indicates that x_f:$t^{2/3}$ reasonably describes the relationship between the front location and time in the deceleration phase for lower slope angles ($\theta = 0$, 2, and 4°), when finding the virtual origin becomes infeasible. Note that for lock-exchange flows, x_f:$t^{2/3}$ indicates the presence of the inertial phase, and a departure from the x_f:$t^{2/3}$ asymptote indicates a transition to a viscous phase (Huppert and Simpson 1980).

For the long-term front location and time relationship at higher slope angles ($\theta = 6$, 8, 10°), we replot the data in Fig. 7(a) using $(x_f + x_0)^{3/2}$ against t and find the best fit equations in the deceleration phase in the power-law form Eq. (6), where x_0 is identified by extrapolating the height versus distance relationship in the deceleration phase and t_0 by extrapolating $(x_f + x_0)^{3/2}$ versus t. It is observed that for higher slope angles, the relationship between front location and time follows the thermal theory power law in the deceleration phase, as shown in Fig. 8 and the inserted fitting equations. Although the conditions $x_f \gg x_0$ and $t \gg t_0$ are not really satisfied, it is observed here that the power law is still very robust and insensitive to the location of virtual origin when the gravity current is not sufficiently far into the deceleration phase, as reported by Maxworthy (2010). With the scaling given in the section entitled "Numerical Formulation," the dimensionless total buoyancy in our formulation is $B_0 = 0.128$, and consequently the determined constant K_M is in the range $2.91 < K_M < 2.98$, where the magnitude is in agreement with Maxworthy (2010). In addition, as seen in the inserted equations, K_M increases slightly as the bottom slope increases, which indicates that more buoyancy accumulates in the front as the bottom slope increases. This will be discussed in the following section.

Fig. 9(a) shows the front velocity history, with a blown-up view for the deceleration phase in Fig. 9(b). The maximum front velocity, occurring at approximately $t = 3{:}4$, appears to increase with the bottom slope. The relationship between the front velocity and time in Fig. 9(b), on a log-log scale, also shows that the asymptote, u_f:$t^{-1/3}$, is a good approximation for the velocity–time relationship for gravity currents on inclined boundaries. The episodic increase in front velocity in the deceleration phase is due to the vortex rollup, during which process the potential energy is converted to kinetic energy temporarily when the center of gravity is lowered (Cantero et al. 2007; Dai et al. 2012). Such an observation applies to all slopes considered here and has been reported to be more amplified in two-dimensional simulations.

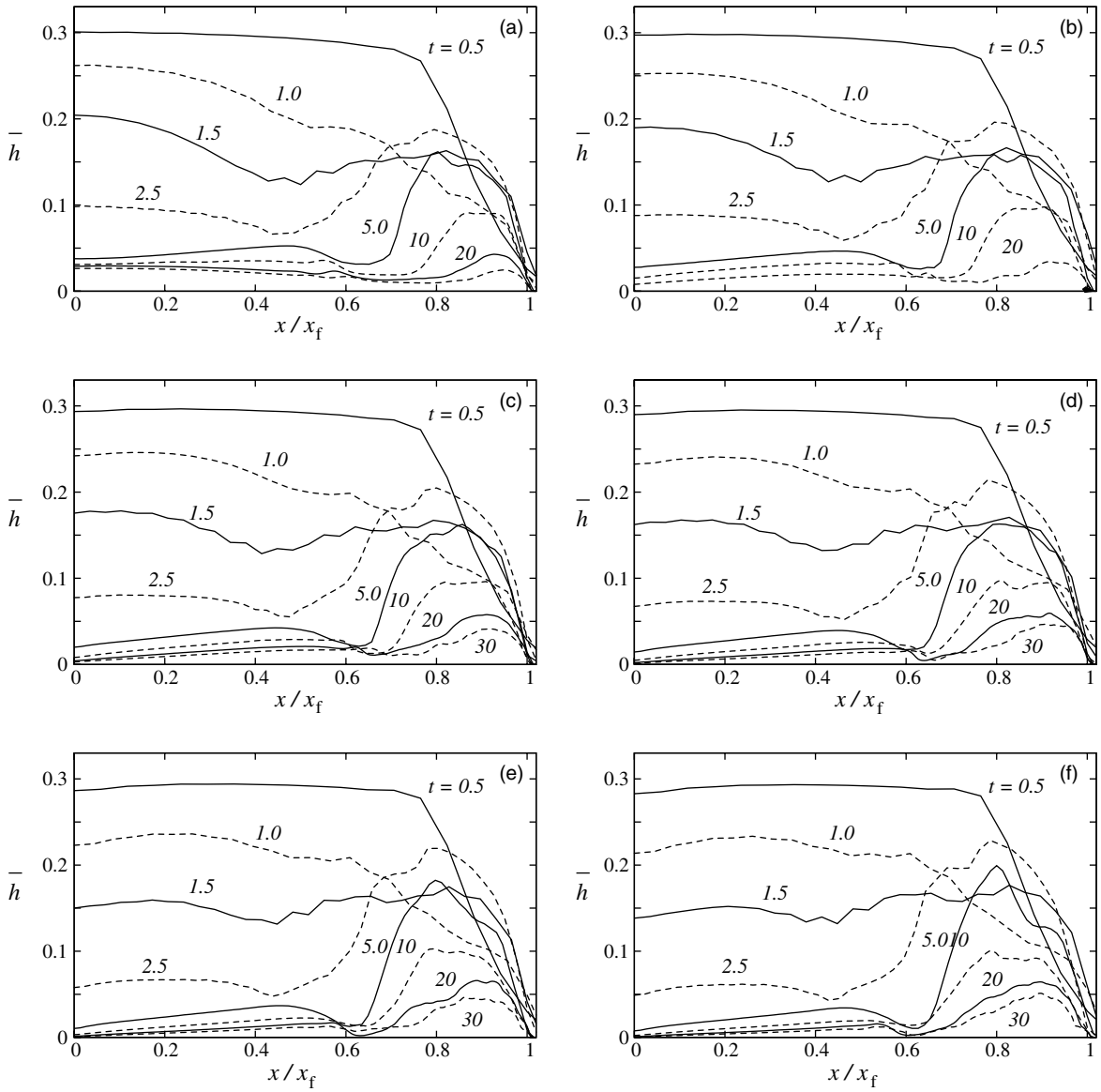

Fig. 5. Structures of gravity current at $R = 10^4$ on different bottom slopes using equivalent heights versus normalized coordinates, x/x_f: (a) $\theta = 0°$; (b) $\theta = 2°$; (c) $\theta = 4°$; (d) $\theta = 6°$; (e) $\theta = 8°$; (f) $\theta = 10°$; corresponding times are indicated in each panel in dimensionless time units

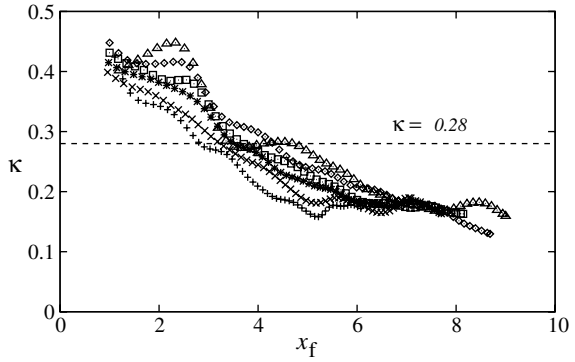

Fig. 6. Aspect ratio of gravity current head, $\kappa = H/L$, versus downslope distance, x_f; dashed line: $\kappa = 0.28$ as approximated in Beghin et al. (1981) for gravity current on a 10° slope; symbols: plus symbol, $\theta = 0°$; x-shaped symbol, $\theta = 2°$; asterisk, $\theta = 4°$; square, $\theta = 6°$; diamond, $\theta = 8°$; triangle, $\theta = 10°$; the aspect ratio of the semielliptical head decreases as gravity current moves downslope

For $\theta = 0°$, the transition from $u_f{:}t^{-1/3}$ to $u_f{:}t^{-5/8}$ indicates the presence of a viscous phase following the inertial phase in lock-exchange flows. Also note that for gravity currents produced from a finite, instantaneous buoyancy source propagating on a slope, the motion is driven by the downslope gravitational force and retarded principally by the entrainment, and the deceleration phase follows the acceleration phase without the presence of a slumping phase, in which the front velocity remains constant. While it may seem that the power-law asymptote describes the front velocity history for all slope angles, it should be remembered that the same velocity asymptote is also implied by the thermal theory as the gravity current is sufficiently far from the virtual origin. Based on the fact that the gravity current has similar structures for lower slope angles ($\theta = 0$, 2, and 4°), as shown in Fig. 4, the consistency between the velocity relation and the power-law asymptote for the lower slope angles is more appropriately addressed by the applicability of the inertial phase asymptote of gravity currents in lock-exchange flows (Huppert and Simpson 1980; Marino et al. 2005).

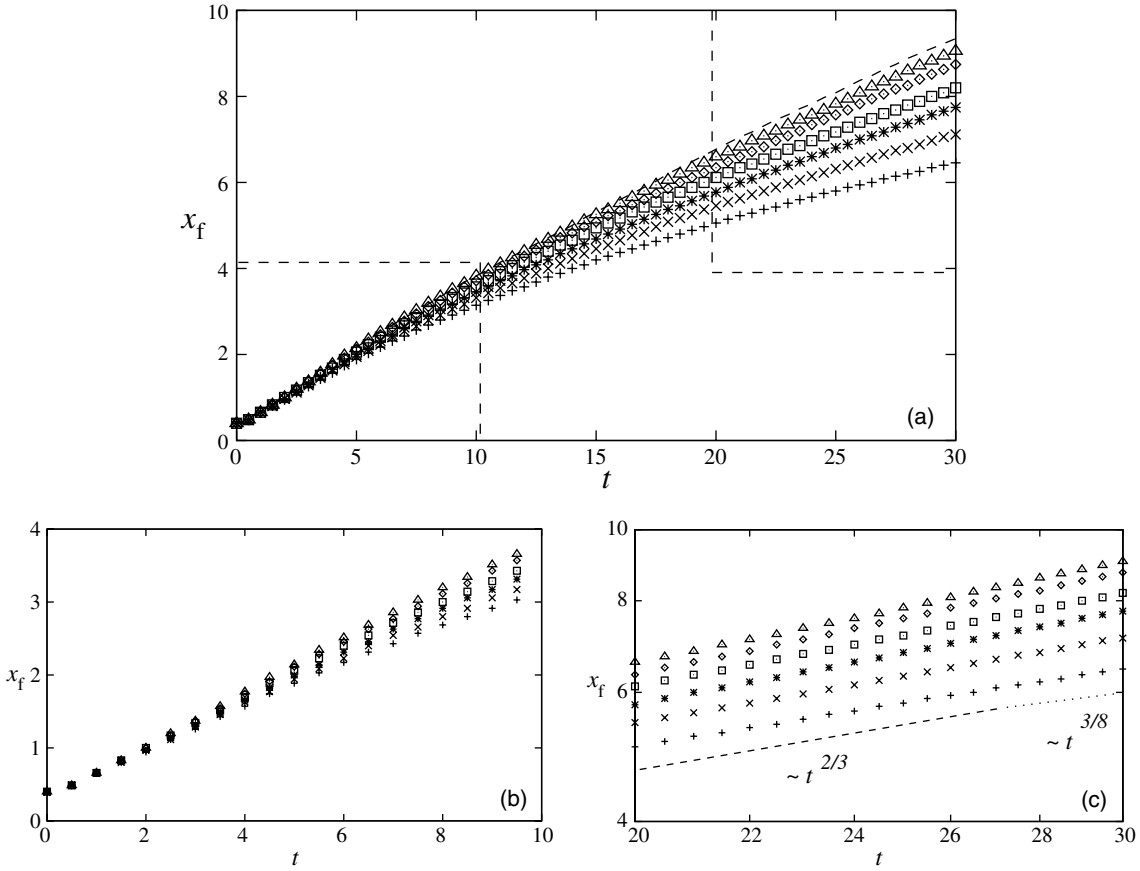

Fig. 7. Front location versus time for gravity currents on different bottom slopes: (a) x_f versus t for whole simulation time $0 \le t \le 30$; (b) blown-up view for acceleration phase; (c) blown-up view for deceleration phase on log-log scale, where x_f:$t^{2/3}$ indicates inertial phase and x_f:$t^{3/8}$ indicates viscous phase in lock-exchange flows (Huppert and Simpson 1980); symbols: plus symbol, $\theta = 0°$; x-shaped symbol, $\theta = 2°$; asterisk, $\theta = 4°$; square, $\theta = 6°$; diamond, $\theta = 8°$; triangle, $\theta = 10°$; dashed line in (a) = simulation with free-slip top boundary on a $\theta = 10°$ slope

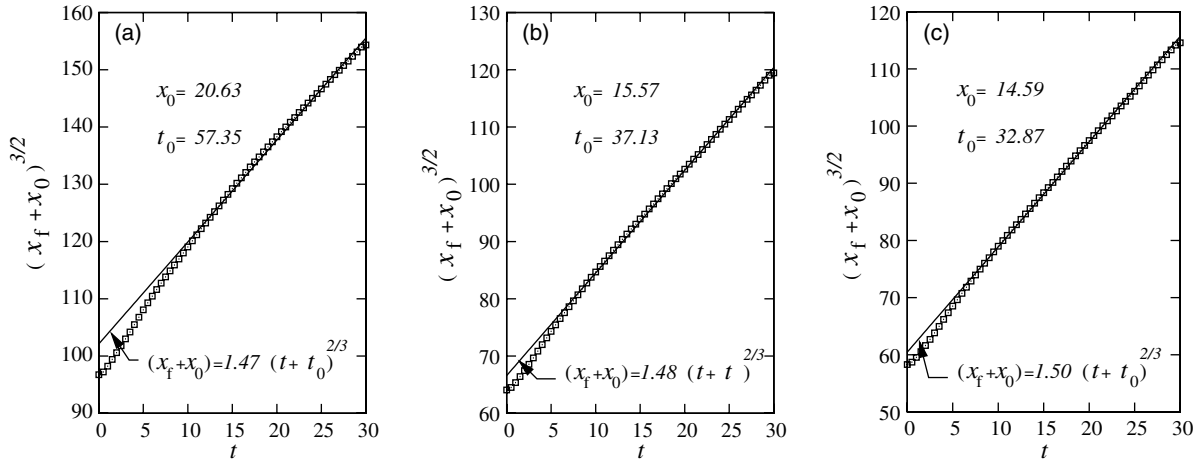

Fig. 8. Front location history, $(x_f + x_0)^{3/2}$ versus t, for higher slope angles; (a) $\theta = 6°$; (b) $\theta = 8°$; (c) $\theta = 10°$; inserted equations are written in form $(x_f + x_0) = K_M B_0^{1/3}(t + t_0)^{2/3}$, which describes the long-term front location and time relationship based on thermal theory

Driving Buoyancy in Head

Now focus will turn to the buoyancy contained in the head, which is understood as the driving force in a gravity current motion. Here the effective buoyancy, B_f, is defined, i.e., the buoyancy contained in the head as

$$B_f = \int_L \bar{h}(x_1, t)dx_1 \tag{19}$$

where the subscript L in the integral denotes that the integration is done exclusively in the head region of extent L. If the head were to

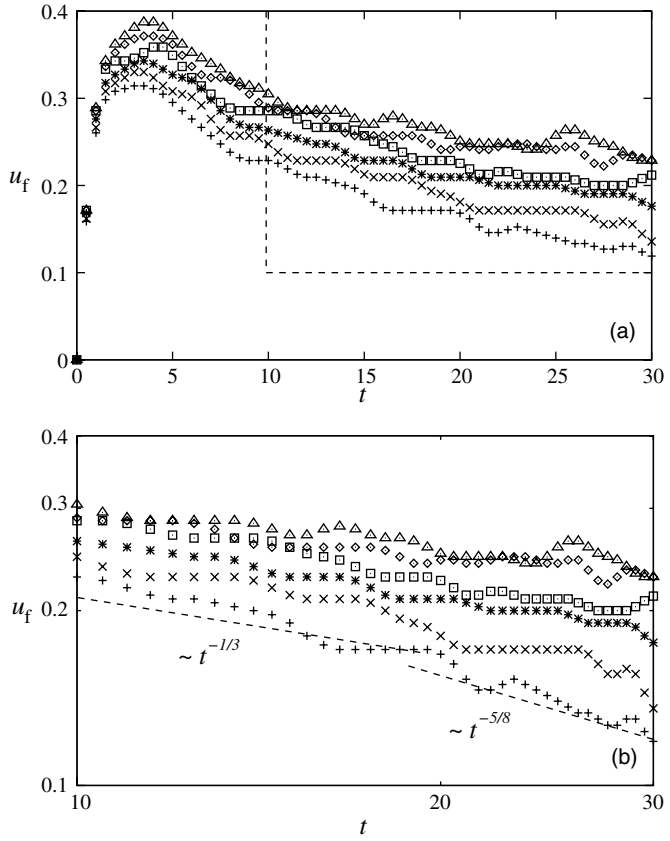

Fig. 9. (a) Front velocity versus time for gravity currents on different bottom slopes; (b) blown-up view of front velocity-distance relationship in deceleration phase, on a log-log scale; in (b), u_f:$t^{-1/3}$ and u_f:$t^{-5/8}$ indicate inertial and viscous phases for gravity currents on horizontal boundary; symbols: plus symbol, $\theta = 0°$; x-shaped symbol, $\theta = 2°$; asterisk, $\theta = 4°$; square, $\theta = 6°$; diamond, $\theta = 8°$; triangle, $\theta = 10°$

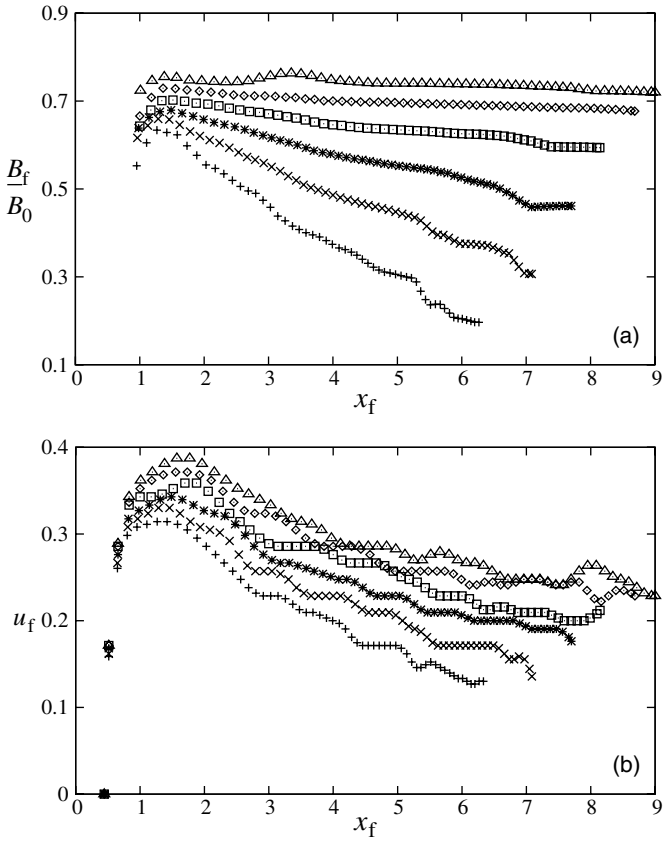

Fig. 10. (a) Effective buoyancy normalized by initial buoyancy, B_f/B_0, versus downslope distance; (b) front velocity u_f versus downslope distance; symbols: plus symbol, $\theta = 0°$; x-shaped symbol, $\theta = 2°$; asterisk, $\theta = 4°$; square, $\theta = 6°$; diamond, $\theta = 8°$; triangle, $\theta = 10°$

contain the total buoyancy, then the effective buoyancy would be identical to the initial buoyancy, i.e., $B_f = B_0$.

Fig. 10(a) shows the effective buoyancy, normalized by the initial buoyancy $B_0 = 0.128$, versus the downslope distance, comparing it with the velocity–distance relationship in Fig. 10(b). When the head is developing as gravity currents propagate downslope, the effective buoyancy increases with downslope distance. Since the equivalent height provides an unambiguous measure of the distribution of heavy fluid in the streamwise direction, it is observed that the buoyancy in the head is fed from behind through the joining tail current, as illustrated in Figs. 4(a–f) prior to t:5. Furthermore, the maximum effective buoyancy also depends on the bottom slope, from 63% of the initial buoyancy at $\theta = 0°$ to 75% at $\theta = 10°$, which indicates that as the bottom slope increases, more heavy fluid tends to accumulate in the head for the slope angles considered here. As shown in Fig. 10(b), in general the effective buoyancy increases (decreases) as the gravity currents are in the acceleration (deceleration) phase, but the maximum front velocity occurs slightly after the maximum effective buoyancy is reached. As described by the linear momentum, the front velocity tends to increase as the driving mechanisms, effective buoyancy and component of gravity in the streamwise direction, intensify. Note that in all the cases considered, the maximum effective buoyancy never reached the total buoyancy, which indicates that a significant portion of heavy fluid was retained in the tail current from the release of gravity currents and never made it to the current head, e.g., at $\theta = 10°$ the head contains at most 75% of the total buoyancy, when the deceleration phase begins.

In the deceleration phase, as shown in Figs. 10(a and b), the effective buoyancy decreases as the gravity currents propagate. Further, the rate of decrease in the effective buoyancy depends on the bottom slope. The head loses buoyancy-containing fluid less rapidly as the bottom slope increases. For lower slope angles ($\theta = 0$, 2, and 4°), the head and tail of the gravity currents are connected, but the relative length of the head diminishes as the gravity currents propagate. As such, the buoyancy contained in the head region decreases, leaving heavy fluid behind in the tail currents. For higher slope angles ($\theta = 6$, 8, and 10°), as shown in Fig. 2, the head separates from the tail of gravity currents, of which the relative length of the head is approximately constant and the loss of buoyancy as in the lower angle cases is not observed.

Conclusions

This paper presented three-dimensional DNSs of gravity currents on different slopes and investigated the influence of bottom slopes on gravity current dynamics. To more accurately model the initiation mechanism of gravity currents in experiments, this study implemented a reflection condition at the midplane such that the released heavy fluid propagated unidirectionally downslope.

As a first approximation in thermal theory, the gravity current head was assumed to maintain a semielliptical shape with a

J. Hydraul. Eng., 2013, 139(6): 593-601

constant height-to-length aspect ratio. It was observed that the aspect ratio could decrease by a factor of over two as the gravity currents propagated. The constant aspect ratio assumption was true only in an average sense.

The maximum front velocity and the maximum effective buoyancy contained in the front both increased as the bottom slope increased. Moreover, the maximum effective buoyancy never reached the total buoyancy, indicating that a significant portion of heavy fluid was constantly kept in the tail current. The maximum effective buoyancy in the head reached approximately 75% of the total released buoyancy for $\theta = 10°$. In the acceleration phase, the tail current connected to and fed buoyancy into the head for all the cases considered in the study. In the deceleration phase, for lower slope angles ($\theta = 0$, 2, and 4°), the tail current continued to join the head and the relative length of the head diminished as the gravity current propagated downslope. For higher slope angles ($\theta = 6$, 8, and 10°), the head disconnected the joining tail current in the deceleration phase and the relative length of the head remained approximately constant. The rate at which gravity current head lost buoyancy-containing fluid also depended on the bottom slope. Effective buoyancy in the head decreased more rapidly for the lower slope angles than for the higher ones. The structures of gravity currents also indicated in the deceleration phase that the buoyancy was left in the tail current for lower slope angles and the tail disconnected the front for higher slope angles, which made it possible to maintain a higher effective buoyancy. It was also found that the front location and time relationship in the deceleration phase followed the thermal theory power law for higher slope angles and for lower slope angles, and a similar power-law asymptote of the inertial phase of gravity currents was observed.

In addition to the preceding observations, the findings in this study also suggest that the slope angle determines the stucture of gravity currents generated from instantaneous sources on a slope and the existence of a threshold slope angle beyond which the front will disconnect the tail current and propagate downslope by itself. Regardless of whether or not an overhaul of the existing thermal theory is warranted, it is clear from the study that the influence of the bottom slope should be carefully evaluated when the thermal theory is in use for the description of gravity currents on sloping boundaries.

Acknowledgments

The author wishes to thank Professor S. Balachandar at the University of Florida for valuable comments at different stages of the work. Computations reported in the study were performed at the National Center for High-Performance Computing in Taiwan. The research was funded by the National Science Council of Taiwan through Projects NSC 98-2218-E-032-007 and NSC 101-2628-E-032-003-MY3. Thanks are also extended to the reviewers for making suggestions that improved the quality of the paper.

References

Allen, J. (1985). *Principles of physical sedimentology*, Allen & Unwin, London.

Batchelor, G. K. (1967). *An introduction to fluid dynamics*, Cambridge University Press, Cambridge, UK.

Beghin, P., Hopfinger, E. J., and Britter, R. E. (1981). "Gravitational convection from instantaneous sources on inclined boundaries." *J. Fluid Mech.*, 107, 407–422.

Birman, V. K., Battandier, B. A., Meiburg, E., and Linden, P. F. (2007). "Lock-exchange flows in sloping channels." *J. Fluid Mech.*, 577, 53–77.

Birman, V. K., Martin, J. E., and Meiburg, E. (2005). "The non-boussinesq lock-exchange problem. Part 2. High-resolution simulations." *J. Fluid Mech.*, 537, 125–144.

Bonometti, T., and Balachandar, S. (2008). "Effect of schmidt number on the structure and propagation of density currents." *Theor. Comput. Fluid Dyn.*, 22(5), 341–361.

Britter, R. E., and Linden, P. F. (1980). "The motion of the front of a gravity current travelling down an incline." *J. Fluid Mech.*, 99, 531–543.

Cantero, M., Balachandar, S., Garcia, M., and Ferry, J. (2006). "Direct numerical simulations of planar and cylindrical density currents." *J. Appl. Mech.*, 73(6), 923–930.

Cantero, M., Lee, J., Balachandar, S., and Garcia, M. (2007). "On the front velocity of gravity currents." *J. Fluid Mech.*, 586, 1–39.

Canuto, C., Hussaini, M., Quarteroni, A., and Zang, T. (1988). *Spectral methods in fluid dynamics*, Springer, Berlin.

Cortese, T., and Balachandar, S. (1995). "High performance spectral simulation of turbulent flows in massively parallel machines with distributed memory." *Int. J. Supercomput. Appl.*, 9(3), 187–204.

Dai, A. (2010). "Note on the generalized thermal theory for gravity currents in the deceleration phase." *Dyn. Atmos. Oceans*, 50(3), 424–431.

Dai, A., Ozdemir, C. E., Cantero, M. I., and Balachandar, S. (2012). "Gravity currents from instantaneous sources down a slope." *J. Hydraul. Eng.*, 138(3), 237–246.

Durran, D. (1999). *Numerical methods for wave equations in geophysical fluid dynamics*, Springer, Berlin.

Ellison, T. H., and Turner, J. S. (1959). "Turbulent entrainment in stratified flows." *J. Fluid Mech.*, 6, 423–448.

Fannelop, T. K. (1994). *Fluid mechanics for industrial safety and environmental protection*, Elsevier, Amsterdam, The Netherlands.

Hartel, C., Meiburg, E., and Necker, F. (2000). "Analysis and direct numerical simulation of the flow at a gravity-current head. I: Flow topology and front speed for slip and no-slip boundaries." *J. Fluid Mech.*, 418, 189–212.

Hopfinger, E. J., and Tochon-Danguy, J. C. (1977). "A model study of powder-snow avalanches." *J. Glaciol.*, 19(81), 343–356.

Huppert, H., and Simpson, J. (1980). "The slumping of gravity currents." *J. Fluid Mech.*, 99, 785–799.

La Rocca, M., Adduce, C., Sciortino, G., and Pinzon, A. B. (2008). "Experimental and numerical simulation of three-dimensional gravity currents on smooth and rough bottom." *Phys. Fluids*, 20(10), 106603.

Marino, B., Thomas, L., and Linden, P. (2005). "The front condition for gravity currents." *J. Fluid Mech.*, 536, 49–78.

Maxworthy, T. (2010). "Experiments on gravity currents propagating down slopes. II: The evolution of a fixed volume of fluid released from closed locks into a long, open channel." *J. Fluid Mech.*, 647, 27–51.

Maxworthy, T., and Nokes, R. I. (2007). "Experiments on gravity currents propagating down slopes. I: The release of a fixed volume of heavy fluid from an enclosed lock into an open channel." *J. Fluid Mech.*, 584, 433–453.

Morton, B. R., Taylor, G. I., and Turner, J. S. (1956). "Turbulent gravitational convection from maintained and instantaneous sources." *Proc. R. Soc. A*, 234, 1–23.

Rastello, M., and Hopfinger, E. J. (2004). "Sediment-entraining suspension clouds: A model of powder-snow avalanches." *J. Fluid Mech.*, 509, 181–206.

Shin, J., Dalziel, S., and Linden, P. (2004). "Gravity currents produced by lock exchange." *J. Fluid Mech.*, 521, 1–34.

Simpson, J. (1997). *Gravity currents*, 2nd Ed., Cambridge University Press, Cambridge, UK.

Williamson, J. H. (1980). "Low-storage Runge-Kutta schemes." *J. Comput. Phys.*, 35, 48–56.